Rotational Single Sheet Tester for Multiaxial Magneto-Mechanical Effects in Steel Sheets

U. Aydin [ID][1], F. Martin [ID][1], P. Rasilo [ID][1,2], A. Belahcen [ID][1], A. Haavisto[1], D. Singh [ID][1], L. Daniel [ID][3], and A. Arkkio [ID][1]

[1]Department of Electrical Engineering and Automation, Aalto University, 00076 Espoo, Finland
[2]Laboratory of Electrical Energy Engineering, Tampere University of Technology, 33101 Tampere, Finland
[3]GeePs|Group of Electrical Engineering—Paris, UMR CNRS 8507, CentraleSupélec, Univ. Paris-Sud, Université Paris-Saclay, Sorbonne Université, 3 rue Joliot-Curie, Plateau de Moulon, F-91192 Gif-sur-Yvette, France

A detailed design of a new rotational single sheet tester device which allows comprehensive multiaxial magneto-mechanical analysis of ferromagnetic sheets is proposed. The challenges that arose during the mechanical and magnetic design phases are addressed. The applicability of the device is tested by performing magneto-mechanical measurements on an M400-50A electrical steel sheet. Results under several multiaxial magneto-mechanical loadings with circular and alternating magnetic flux densities are reported. It is shown that the effect of multiaxial stress on iron losses can be much more significant than that of uniaxial stress.

Index Terms— **Core losses, iron losses, magneto-mechanical effects, multiaxial stress, single sheet tester.**

I. INTRODUCTION

FERROMAGNETIC materials are widely used in many electromagnetic applications such as electrical machines and transducers. In most of these devices, the material is subject to multiaxial mechanical stresses that are caused by manufacturing processes or operating conditions [1]–[6]. In addition, the orientation of the magnetic field and stress may vary in the material, since for instance, in three-phase transformers and rotating electrical machines both rotating and alternating flux conditions occur. On the other hand, it is known that the mechanical stress has strong influence on the magnetic properties of ferromagnetic materials [7]–[22]. Previous studies have shown that the performance of electrical machines is affected significantly by the complex multiaxial magneto-mechanical loadings that occur in the material [23]–[29]. Therefore, it is evident that the characterization of the magnetic properties of electrical steel sheets under multiaxial loadings is needed in order to design more efficient devices. Especially the effect of stress on core losses should be studied in detail.

Single sheet testers are widely used for magneto-mechanical characterization of electrical steel sheets. For instance, in [7]–[11], the magnetic behavior of electrical steel sheets is studied under uniaxial stress applied parallel to the alternating magnetic field. In [12]–[16], the effect of uniaxial stress is studied under rotating flux conditions. Biaxial magneto-mechanical tests have been performed in [17]–[20] using cross-shaped specimens under alternating flux conditions. Even though these biaxial tests can provide a deeper understanding of multiaxial magneto-mechanical behavior compared to uniaxial tests, they do not provide control for arbitrary flux waveform and in-plane stress tensors in the material which occur in electrical machines. A device that has the ability to apply an arbitrary in-plane stress tensor and flux density, using a specimen that has eight legs, is reported in [21] and [22]. They reported magneto-mechanical experimental results under up to 0.6 T peak induction and ±30 MPa maximum stress levels.

In this paper, a rotational single sheet tester (RSST) device that provides a possibility of comprehensive analysis of multiaxial magneto-mechanical behavior of ferromagnetic sheets is introduced. Details of the design phases are explained, and the challenges that arose during the design phases are addressed. The measurement system and control procedures for stress and flux density waveform are detailed. Magneto-mechanical measurements under circular and alternating flux densities up to 1.2 T and under ±30 MPa multiaxial in-plane stresses on an M400-50A non-oriented electrical steel sheet are performed and reported.

II. DESIGN OF THE ROTATIONAL SINGLE SHEET TESTER

In order to analyze the effect of mechanical stress on the magnetic behavior of the material accurately, uniform stress and magnetic field distributions need to be created in an area large enough for performing the measurements. Therefore, the aim was to design a sample geometry that fulfills these requirements and which allows arbitrary stress and magnetization control.

The flat geometry of the electrical steel sheets allows in-plane study of the geometry which means the stress tensor $\boldsymbol{\sigma}$ has three variables to be controlled and the tensor can be written as $\boldsymbol{\sigma} = [\,\sigma_{xx}\ \sigma_{yy}\ \sigma_{xy}\,]^{\mathrm{T}}$ in Voigt notation. Previously, we have shown in [30] that it is possible to control each component of $\boldsymbol{\sigma}$ using a six-leg sample geometry. The calculation will be repeated here for the sake of clarity. Take the sample geometry shown in Fig. 1 and assume an isotropic linear elastic material. In order to have the desired in-plane stress tensor at the measurement area that is located at the central region of
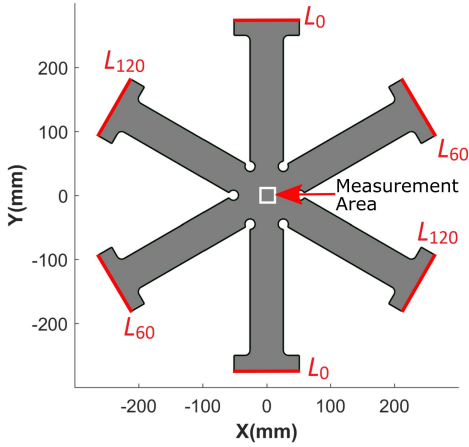
Fig. 1.   Sample geometry.

the sample, the required mechanical loadings for each leg pair can be calculated by constructing a linear set of equations using the following procedure.

1) An initial mechanical loading p_{ini} is applied only to the L_0 leg pair and an in-plane stress tensor in the central area is obtained as

$$\boldsymbol{\sigma}_{0^\circ} = \begin{bmatrix} \sigma_{0^\circ\text{xx}} & \sigma_{0^\circ\text{xy}} \\ \sigma_{0^\circ\text{xy}} & \sigma_{0^\circ\text{yy}} \end{bmatrix}. \tag{1}$$

2) In order to get reference stress tensors at the central region for legs L_{60} and L_{120}, a coordinate transformation is applied to (1) using coordinate transformation matrix $\mathbf{Q}_\theta$ for angles $\theta = 60^\circ$ and $\theta = 120^\circ$ as

$$\mathbf{Q}_\theta = \begin{bmatrix} \cos\theta & \sin\theta \\ -\sin\theta & \cos\theta \end{bmatrix} \tag{2}$$

$$\boldsymbol{\sigma}_\theta = \mathbf{Q}_\theta \cdot \boldsymbol{\sigma}_{0^\circ} \cdot \mathbf{Q}_\theta^{\text{T}}. \tag{3}$$

3) Let us define the desired in-plane stress tensor in the central region as $\boldsymbol{\sigma}_{\text{ref}}$ and required mechanical loadings to be applied to L_0, L_{60}, and L_{120} leg pairs as p_{0°, p_{60°, and p_{120°, respectively. Since linear elasticity is assumed, a linear relation between p_{0°, p_{60°, p_{120°, and p_{ini} can be used to set the following equation:

$$\boldsymbol{\sigma}_{\text{ref}} = \boldsymbol{\sigma}_{0^\circ} \cdot \frac{p_{0^\circ}}{p_{\text{ini}}} + \boldsymbol{\sigma}_{60^\circ} \cdot \frac{p_{60^\circ}}{p_{\text{ini}}} + \boldsymbol{\sigma}_{120^\circ} \cdot \frac{p_{120^\circ}}{p_{\text{ini}}}. \tag{4}$$

Equation (4) can be written in a more consistent form as

$$\begin{bmatrix} \sigma_{\text{ref,xx}} \\ \sigma_{\text{ref,yy}} \\ \sigma_{\text{ref,xy}} \end{bmatrix} = \frac{1}{p_{\text{ini}}} \cdot \begin{bmatrix} \sigma_{0^\circ\text{xx}} & \sigma_{60^\circ\text{xx}} & \sigma_{120^\circ\text{xx}} \\ \sigma_{0^\circ\text{yy}} & \sigma_{60^\circ\text{yy}} & \sigma_{120^\circ\text{yy}} \\ \sigma_{0^\circ\text{xy}} & \sigma_{60^\circ\text{xy}} & \sigma_{120^\circ\text{xy}} \end{bmatrix} \cdot \begin{bmatrix} p_{0^\circ} \\ p_{60^\circ} \\ p_{120^\circ} \end{bmatrix}. \tag{5}$$

Solution of this system for p_{0°, p_{60°, and p_{120° yields the required loadings to be applied to the leg pairs L_0, L_{60}, and L_{120} in order to obtain the arbitrary in-plane stress tensor $\boldsymbol{\sigma}_{\text{ref}}$ at the central region. Mechanical stresses should be applied to each leg pair independently to ensure the homogeneity of stress distribution. A negligible displacement in the central point of the sample is preferred so that six actuators are needed. It is worth mentioning that the same principle can be applied to obtain an in-plane strain tensor as well. The above-mentioned calculation was given in order to demonstrate that it is possible to obtain an arbitrary in-plane stress tensor

using six-leg geometry by assuming an isotropic material. In practice, having an isotropic material might not be possible. Therefore, this procedure will not be used directly for the control of the mechanical actuators.

The tips of the legs in the sample geometry were designed having T-shapes to ease the clamping of the sample for stress application. The maximum magnitude of the stress that can be applied to the legs is limited by the buckling of the sample under compressive loading. To maximize the compressive stress without facing the buckling issue, the ratio of the sample length to its thickness should be as low as possible. On the other hand, the sample should be long enough to obtain low values of a demagnetizing factor. In addition, the narrower widths close to the central region in the sample geometry help obtaining higher mechanical stress in the measurement area compared to the sample geometry without these regions, when the same mechanical loadings are applied to the tips of the legs.

In single sheet testers that adopt magnetization yokes, the systems to magnetize the specimen can be categorized into vertical and horizontal magnetization systems depending on the penetration angle of the flux to the sample. In the vertical and horizontal magnetization systems, the penetration direction of the flux to the specimen is perpendicular and parallel to the specimen plane, respectively. In this paper, a horizontal magnetization system is adopted due to its advantages over vertical systems. For instance, the formation of eddy currents where the flux penetrates the sample can be minimized using horizontal yoke systems. This helps to reduce the angular bending of the flux. Using a correct horizontal yoke geometry can also reduce the stray fluxes between the yokes and the sample greatly [31], [32]. Another advantage of a horizontal magnetizing system is that the sample installation can be considerably simpler since the magnetizing system is usually fixed. Six magnetization coils that are wound around magnetizing yokes are placed between each leg, which means that the space for the magnetization system should be taken into account when determining the sample diameter.

All these factors were considered to determine the sample diameter. Before finalizing the sample geometry, in order to ensure the stress and magnetic field homogeneity at the central region, several sample geometries were simulated using the finite-element method. For simulating the mechanical part, 2-D plane stress approximation was used and several mechanical loading configurations were simulated. For simulating the magnetic part, a 2-D approximation that assumes the same thickness for all the geometry leads to inaccurate field calculation results since in reality, the magnetizing yokes are much thicker than the sample. For this reason, the magnetic part was simulated by using 3-D magnetic vector potential formulation. Considering the simulation results on several sample geometries, the geometry shown in Fig. 1 has resulted in sufficient homogeneity of the magnetic flux density and stress distributions. In a measurement area of $20 \times 20 \text{ mm}^2$, the maximum relative standard deviation of the stress was found to be 4.38%. For the magnetic flux density, this value was 2.74% and obtained at the instant shown in Fig. 2.
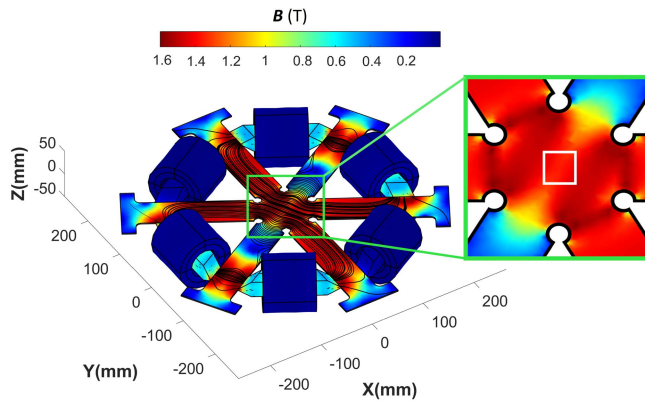
Fig. 2. Distribution of norm of **B** at the instant when the highest variation of norm of **B** is observed in the measurement area. Black lines: flux lines.

It is now established that using a sample geometry as shown in Fig. 1, it is possible to obtain any in-plane stress tensor with negligible displacement in the measurement area. In addition, with proper control, the sample can be magnetized with arbitrary magnetization waveform in the measurement area. This means that any orientation between in-plane stress and magnetization can be obtained using a single sample. On the contrary, in order to achieve this using a cross-shaped sample geometry with two-axis stress application, one would need to perform experiments on several samples cut along different orientations with respect to the rolling direction. In addition, with such a two-axis system, it is not possible to control the shear component of the in-plane stress arbitrarily.

After the sample geometry was finalized, the components for applying magneto-mechanical loading were determined. In order to apply mechanical stresses, a type T90 Thomson ball screw guide was driven by an HWIN 750 W servomotor that is coupled to a Girard servo gearbox with a gear ratio of 60:1. The servomotor is controlled by an HIWIN D2-series servo drive. This system was chosen because of its high precision, simple controllability, and its ability of applying dynamic stresses up to 40 Hz frequency. In order to measure the applied force, a Tecsis F2301 load cell was mounted to the actuator. Six of these configurations are adopted to apply mechanical stresses to each leg of the sample shown in Fig. 1. The clamping of the sample to the actuation system was done by screwing non-magnetic plates on the top of T-shaped ends. To avoid buckling under compressive stress, the sample can be reinforced from the top and the bottom by non-magnetic plates. Since the specimen was placed on a non-magnetic sample holder that was mounted on a steel frame, the reinforcing plates were added on the top of the sample and pressure was applied by clamping devices to the reinforcing plates. Friction should be minimized between the sample, sample holder, and reinforcing plates to ensure free movement of the sample during application of magneto-mechanical loading. This can be done by applying low viscosity oil on each side of the sample before placing it into the sample holder. With the current setup, the buckling of the sample starts when a compressive loading greater than 24 MPa is applied to the sample leg tips. The location of the buckling is observed to be close to the
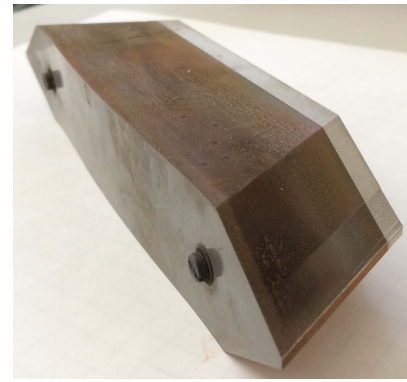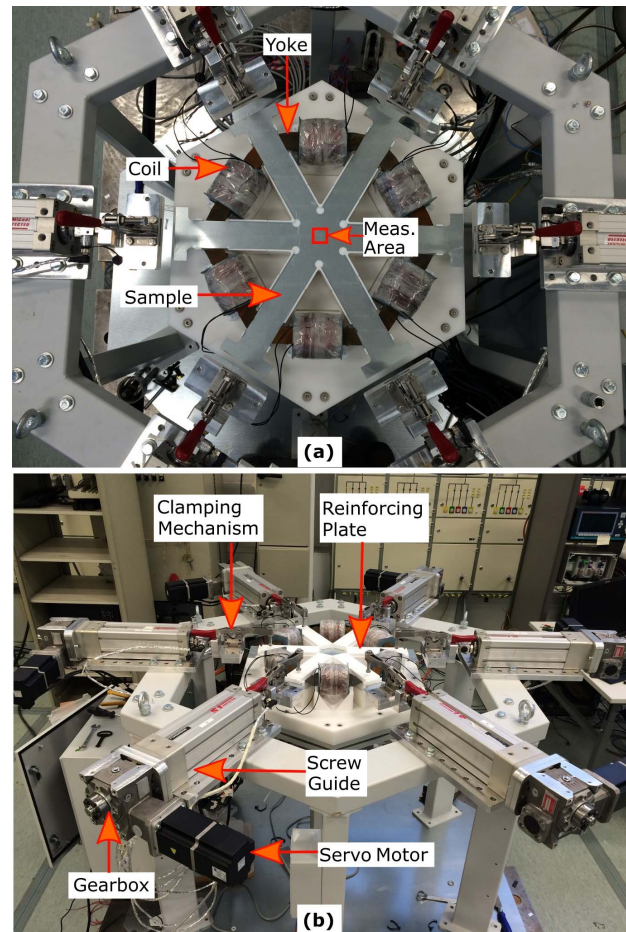

Fig. 3. Magnetizing yoke.

Fig. 4. RSST device is shown (a) from top and (b) as a whole.

coupling location between the mechanical actuators and the sample.

In order to obtain arbitrary magnetization in the measurement area, coils are supplied by a controlled three-phase voltage supply. Each coil has a winding area of 23×89 mm^2, and they contain 2000 turns of 0.8 mm enameled copper wire. To reduce the leakage flux, magnetizing yoke parts were designed to have declining faces where they reach the sample sheet. The geometry of the yoke is shown in Fig. 3. As yoke material, grain-oriented electrical steel was used to maximize the performance. After this step, the design phase was completed. The finalized setup is shown in Fig. 4.
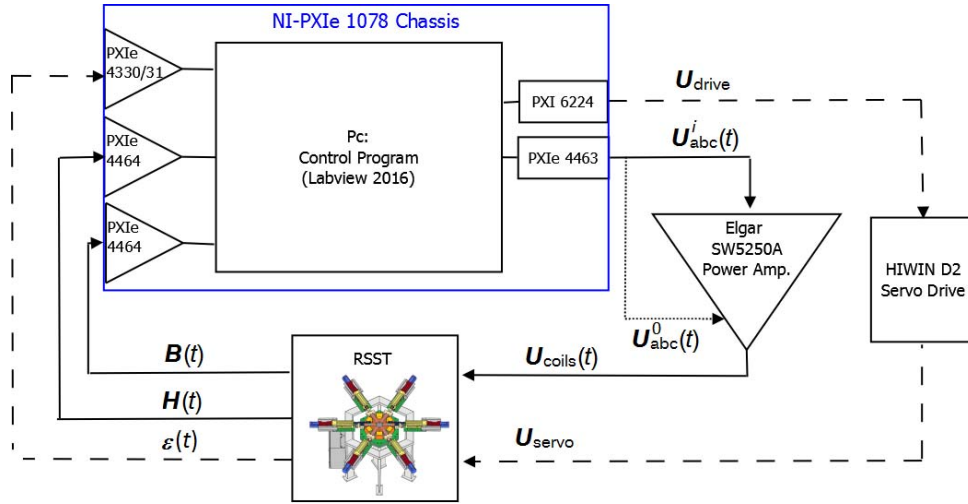
Fig. 5. Schematic of the measurement system.

III. Measurement System

A. Sample Preperation and Sensors

The mechanical strain ε in the central region of the sample is measured using a rosette type strain gauge with $0° - 45° - 90°$ orientation and with 10 mm diameter. Afterward, the stress is calculated using the well-known plane stress formulation of Hooke's law. Before attaching the strain gauge, the insulation around the measurement area is removed by using fine sandpaper. Alignment of the sensor is critical and should be done carefully. After the strain gauge is placed, a protective coating paste is applied on top of it.

There are two common methods that have been used to measure magnetic flux density B on single sheet testers. These are B-coil and needle probe methods [31], [32]. B-coil method usually involves drilling holes to the sample for winding search coils with several turns. In order to minimize the effect of the hole on the homogeneity of the flux distribution, the hole diameter should be as small as possible. The needle probe method is non-destructive. However, it is prone to errors since the signal obtained from the needles is very small and can be noisy. In this paper, the B-coil method was preferred for B measurements due to its reliability. The diameter of the hole drilled for the coils is 0.7 mm. Two search coils of four turns each were placed at the central region of 20×20 mm^2 area perpendicular to each other. After the coils were wound, in order to protect the wire insulation, a silicon protective paste was applied inside the holes.

For the magnetic field strength H measurements, tunneling magnetoresistive sensors can be used [33]. These sensors are able to measure dc field as well as alternating field. However, they measure the field rather locally and further investigation on their performance for measuring rotational fields is needed. In this paper, H-coils were used for H measurements, which is a common method [31], [32]. The coils were calibrated using an air core solenoid. The placement of the H-coil to the sample surface should be done carefully to avoid large misalignments which can cause measurement errors especially for the losses [34], [35].

B. Data Acquisition System

The data acquisition system consists of the following components.
1) A bridge amplifier module NI-PXIe 4330/4331 for strain measurements.
2) Two analog input modules NI-PXIe 4464 for B and H measurements.
3) Two analog output modules NI-PXIe 4463 for delivering voltage output to the power amplifier.
4) A multifunctional I/O module NI-PXI 6224 for generating digital output for servo drive control.

All these modules are connected to NI-PXIe 1078 chassis which includes an internal computer. The coils are connected to three-phase Elgar SW5250A power amplifier which can be controlled externally. The overall measurement system is illustrated in Fig. 5.

C. Measurement Procedure and Waveform Control

The measurement procedure starts with applying a pre-stress to the sample. This is done by controlling the servo drive with digital I/O. The servo drive is programmed such that when it receives $U_{\text{drive}} = 5$ V transistor–transistor logic level, it drives the servomotor by a pre-determined displacement. In order to achieve the desired stress tensor at the central region, stress is calculated using simultaneously measured strain and each servo is controlled to displace accordingly. After the stress control is done, the servomotors are locked and the control for flux density starts. It is worth noting that when the sample is magnetized, magnetostriction causes small variations on the total strain. Since the sample ends are locked, magnetostriction adds additional stress to the sample. However, its amplitude is very small compared to the elastic stress.

The control of flux density starts with amplitude correction and it is followed by the waveform control. The amplitude correction is performed to bring the amplitude of the flux density close to the reference one. The aim of the waveform control is to provide correct voltage waveform to the magnetizing coils in order to obtain the desired flux density waveforms along

the both rolling ($B_x(t)$) and transverse ($B_y(t)$) directions in the measurement area. In this paper, the aim is to obtain sinusoidal $B_x(t)$ and $B_y(t)$.

The procedure starts by sending an initial three-phase balanced sinusoidal voltage $U^0_{abc}(t)$ to the power amplifier to be amplified and supplied to the coils. The amplitudes of the initial voltages are chosen to be low to avoid high inrush currents. Then, the control program in LabVIEW environment starts. Since the final aim is to control $B_x(t)$ and $B_y(t)$, Clarke transformation is applied to the three-phase coil supply voltages in order to reduce the three-phase coordinate system abc to an equivalent two-phase coordinate system $\alpha\beta$ by

$$
\underbrace{\begin{bmatrix} U^0_\alpha(t) \\ U^0_\beta(t) \\ 0 \end{bmatrix}}_{U^0_{\alpha\beta}(t)} = \frac{2}{3} \underbrace{\begin{bmatrix} 1 & -\frac{1}{2} & -\frac{1}{2} \\ 0 & \frac{\sqrt{3}}{2} & -\frac{\sqrt{3}}{2} \\ \frac{1}{2} & \frac{1}{2} & \frac{1}{2} \end{bmatrix}}_{T} \cdot \underbrace{\begin{bmatrix} U^0_a(t) \\ U^0_b(t) \\ U^0_c(t) \end{bmatrix}}_{U^0_{abc}(t)}. \quad (6)
$$

After the Clarke transformation, in order to obtain the reference flux density waveforms along rolling ($B_{x,ref}(t)$) and transverse ($B_{y,ref}(t)$) directions, respective voltages $U_\alpha(t)$ and $U_\beta(t)$ are controlled simultaneously in an iterative manner. The iteration steps are denoted with superscripts i. In the following section, for simplicity, we will give equations for controlling $U_\alpha(t)$ only. First, the amplitude correction is applied using

$$
\epsilon^i_{x,amp} = \frac{\max(B^i_x(t))}{\max(B^i_{x,ref}(t))} \quad (7)
$$

$$
U^{i+1}_\alpha(t) = \frac{U^i_\alpha(t)}{\epsilon^i_{x,amp}} \quad (8)
$$

where $B^i_x(t)$ is the measured flux density waveform along rolling direction, which is averaged over the number of periods in the ith iteration. Note that each iteration lasts 1 s regardless of the supply frequency. $U^i_\alpha(t)$ is the control signal in $\alpha\beta$ frame at the ith iteration and $U^{i+1}_\alpha(t)$ is the corrected signal at the next iteration. The ratio given in (7) is also calculated for obtaining $\epsilon^i_{y,amp}$ by comparing $B^i_y(t)$ to $B^i_{y,ref}(t)$. Then, the same procedure above is applied to correct the amplitude of $B_y(t)$ by controlling $U_\beta(t)$ as well. Before supplying the coils with corrected voltages, $U^{i+1}_\alpha(t)$ and $U^{i+1}_\beta(t)$ are transformed to abc frame by using inverse Clarke transform which can be written as

$$
U^{i+1}_{abc}(t) = T^{-1} \cdot \underbrace{\begin{bmatrix} U^{i+1}_\alpha(t) \\ U^{i+1}_\beta(t) \\ 0 \end{bmatrix}}_{U^{i+1}_{\alpha\beta}(t)} \quad (9)
$$

where $U^{i+1}_{abc}(t)$ is the corrected three-phase supply voltage waveform for coils in abc frame. This process is iterated until the values of $\epsilon^i_{x,amp}$ and $\epsilon^i_{y,amp}$ are below a pre-set tolerance. Note that the amplitude control is done only once at the beginning of the control process in order to start the waveform control with reasonable initial flux density amplitude.

After the amplitude control is terminated, the waveform control starts. Similar to the amplitude correction, the transformation of three-phase coil supply voltages from abc frame to $\alpha\beta$ frame using Clarke transformation is first performed. Then, the measured flux density waveforms are compared to the reference ones and the voltage waveforms are corrected in the $\alpha\beta$ frame. Waveform correction for $U^i_\alpha(t)$ is performed by

$$
U^{i+1}_\alpha(t) = U^i_\alpha(t) + A_1 \int \left(B^i_x(t) - B^i_{x,ref}(t) \right) dt \\ + A_2 \left(B^i_x(t) - B^i_{x,ref}(t) \right) \quad (10)
$$

where A_1 and A_2 are the coefficients of the waveform controller and they are chosen to be constants in this paper. The first two terms on the right-hand side of (10) are based on the principle explained in [36]. It has been observed that adding the last term increased the convergence speed slightly. The procedure shown in (10) is also applied for $U^i_\beta(t)$ by comparing $B^i_y(t)$ to $B^i_{y,ref}(t)$ and corrected signal $U^{i+1}_\beta(t)$ is obtained. Before sending the corrected signal, 30 periods of the previous signal are supplied to the coils. This helps for mitigating the effect of demagnetization field. After the waveform correction is performed in $\alpha\beta$ frame, the control signal matrix $U^{i+1}_{\alpha\beta}(t)$ is formed and inverse Clarke transformation is applied to it for obtaining corrected coil voltages in abc frame $U^{i+1}_{abc}(t)$ as shown in (9). The error of the measured $B^i_x(t)$ is calculated at each iteration by

$$
\epsilon^i_{x,wav} = \frac{\left\| B^i_x(t) - B^i_{x,ref}(t) \right\|}{\left\| B^i_{x,ref}(t) \right\|}. \quad (11)
$$

Same error calculation is also done for obtaining $\epsilon^i_{y,wav}$ by comparing $B^i_y(t)$ to $B^i_{y,ref}(t)$. The waveform control is iterated until the convergence criteria $\epsilon^i_{x,wav} < 1\%$ and $\epsilon^i_{y,wav} < 1\%$ are met. The control algorithm is shown as a flowchart in Fig. 6. If needed, higher accuracy of the waveform control can be reached for instance by tuning the coefficients A_1 and A_2 using various methods instead of using constant values [37], [38].

IV. RESULTS AND DISCUSSION

Rotational measurements have been done under circular magnetic flux density with five different magnitudes of 0.25, 0.5, 0.75, 1.0, and 1.2 T and under several static stress states. In addition, the stressed sample is magnetized with sinusoidal magnetic flux density with 1.2 T amplitude along only rolling (x) or transverse (y) directions. Measurement frequency was 10 Hz for all the cases. The stresses applied are uniaxial stress along the x- and y-directions, equibiaxial stress, and pure shear stress. In this paper, the equibiaxial and pure shear stress are expressed as $\sigma = [\sigma\ \sigma\ 0]^T$ and $\sigma = [\sigma\ -\sigma\ 0]^T$, respectively. The magnitude of σ varies from −30 MPa (compression) to 30 MPa (tension) with 10 MPa intervals. The studied stress states are plotted in Fig. 7.

A. Rotating Magnetization Results

Results under zero stress, uniaxial, equibiaxial, and pure shear stress states where $\sigma = \pm 30$ MPa and under 1 T induction level for clockwise (CW) rotation of the field are
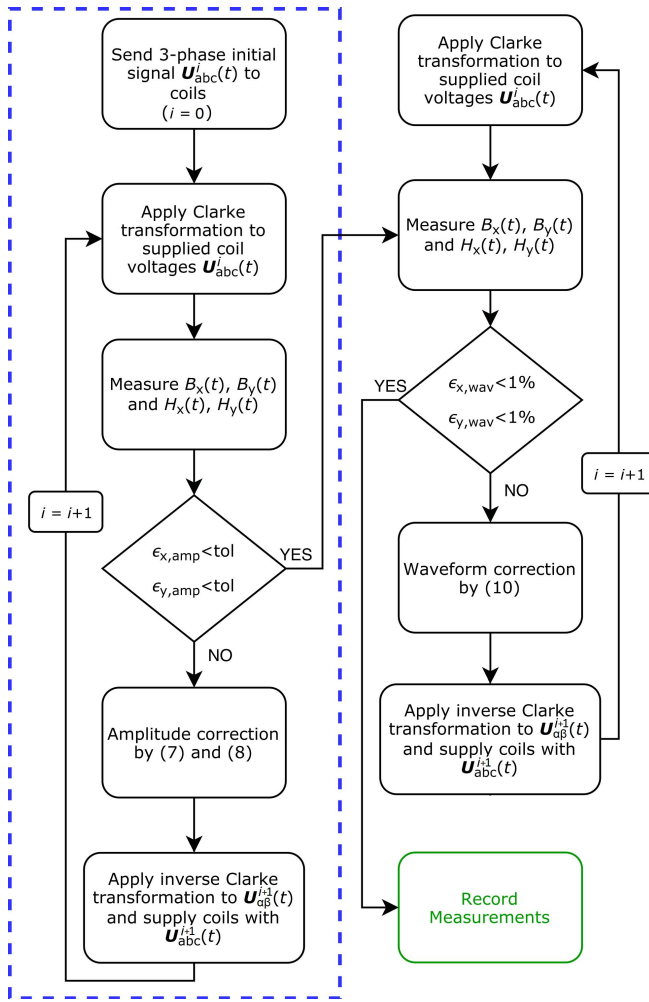
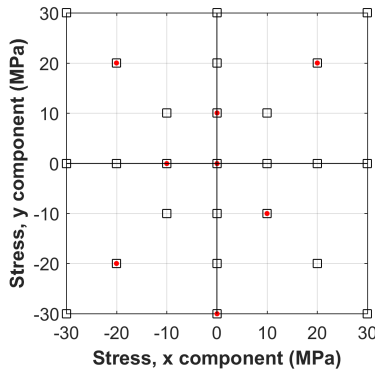Fig. 6. Flux density control algorithm flowchart. Initialization step is marked with dashed rectangle.

Fig. 7. Studied stress states.

Fig. 8. Measured B- and H-loci for CW rotation of the field under 1 T induction level and several stress states. (a) B-loci for each case. (b) H-loci under zero and uniaxial stress along rolling direction. (c) H-loci under zero and uniaxial stress along transverse direction. (d) H-loci under zero and equibiaxial stress. (e) H-loci under zero and pure shear stress.

shown in Fig. 8. Uniaxial stress on both rolling (x) and transverse (y) direction affects the material more than the equibiaxial stress, whereas the effect of pure shear stress on the H-loci is considerably more than that of uniaxial and equibiaxial stress states. The effect of stress on the magnetic anisotropy can be clearly seen. It is known that the application of a low uniaxial tension along a direction improves the susceptibility along the same direction and deteriorates along the direction perpendicular to the stress application direction.
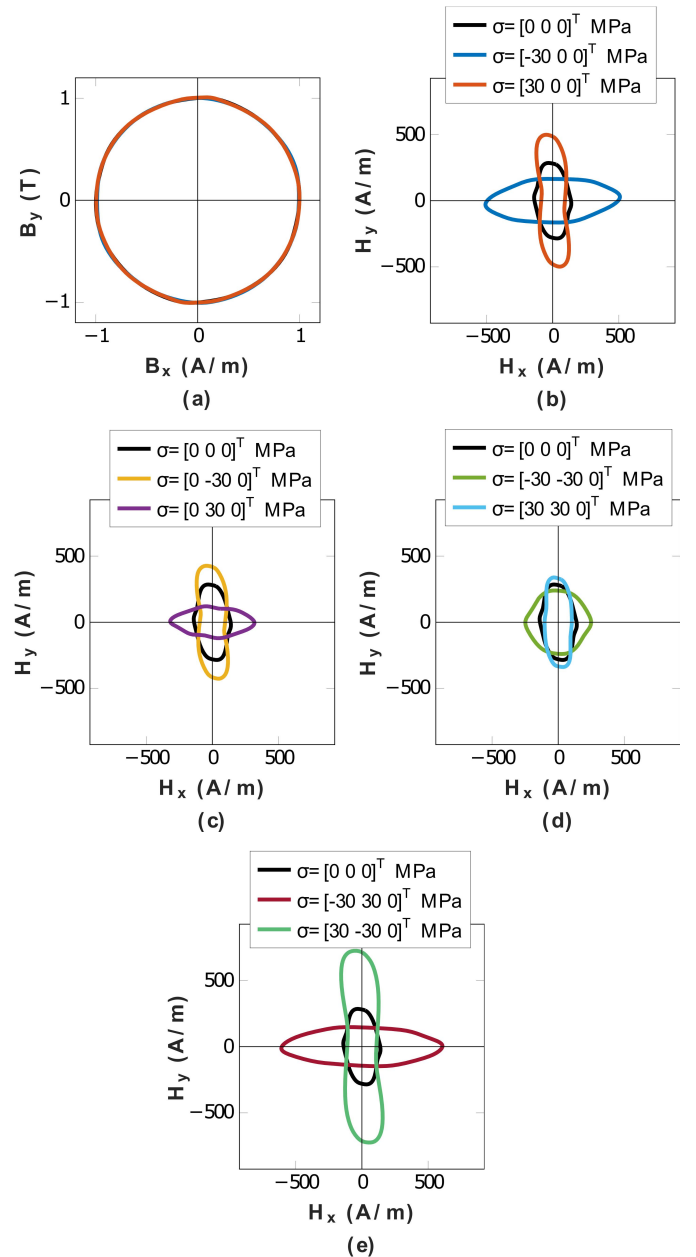
Low uniaxial compressive stress, on the other hand, deteriorates the susceptibility at the direction it is applied to and improves it at the direction perpendicular to the stress application direction. Therefore, the pure shear case that is a non-linear combination of both uniaxial compression and tension enhances the effect of compressive stress on the magnetic behavior. This can be clearly seen by comparing the measurements under $\boldsymbol{\sigma} = [-30\ 0\ 0]^T$ from Fig. 8(b) to $\boldsymbol{\sigma} = [-30\ 30\ 0]^T$ from Fig. 8(e), for instance. Similar results have been reported in [16], [21], and [22].

In order to analyze the material behavior under multiaxial stress further, the root-mean-square (rms) value of the norm of $\boldsymbol{H}$ vector ($\|\boldsymbol{H}\|_{\mathrm{rms}}$) under 1 T flux density and under each
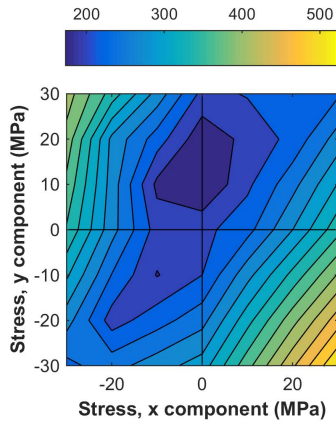
Fig. 9.   RMS value of $\boldsymbol{H}$ vector length under 1 T circular induction and each measured stress state.
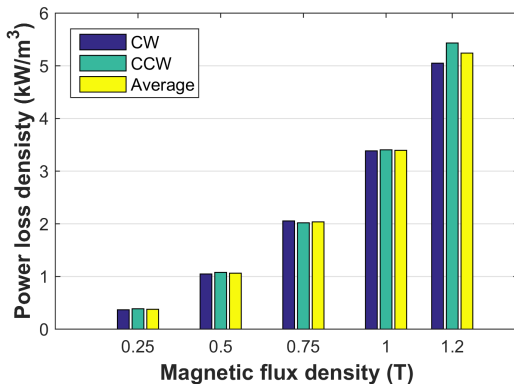

Fig. 10.   Measured CW, CCW, and averaged power loss densities under zero stress and circular flux density at different amplitudes.

measured stress state is shown in Fig. 9. $\|\boldsymbol{H}\|_{\mathrm{rms}}$ represents the rms magnetization current that would be needed to magnetize the sample for obtaining 1 T at each direction. Considering multiaxial stress states, equibiaxial stress shows the least effect on $\|\boldsymbol{H}\|_{\mathrm{rms}}$, whereas the pure shear stress affects it strongly. It is worth noticing that the applied uniaxial stress along rolling direction shows different effects on the material compared to when it is applied along the transverse direction. This behavior is due to the initial anisotropy of the material and it is mainly related to crystallographic texture [39]. Similar measurement results under rotational field are also reported in [14], [15], and [21].

In Fig. 10, the measured power loss densities per cycle under zero stress and under each measured flux density amplitude for CW, counterclockwise (CCW) rotation of the field, and the average of these two are shown for comparison purpose. The highest difference between CW and CCW losses are observed at 1.2 T with 7% relative difference. Ideally, with perfectly aligned H-coils, losses for CW and CCW rotation of the field should be very close to each other. However, aligning the H-coils perfectly is a very challenging task, especially for complex measurement setups. In order to calculate the misalignment angle of the H-coils, the approach presented in [40] is followed. Since the holes for B-coils were drilled with precision machinery, B-coils are assumed to be orthogonal. Under this assumption, the misalignment angle of the H-coils

was calculated to be $-0.07°$. Since the misalignment angle is very small, it is assumed that averaging of CW and CCW losses provide a very close approximation to the actual losses [31], [40]–[42]. It is worth mentioning that precise error analysis for sensor misalignment using the field and loss measurements is a difficult task due to the repeatability error of the measurements. Indeed, it is seen in Fig. 10 that the sign of the difference between CW and CCW losses is positive for some cases and negative for the others, which indicates that the uncertainty of the measurements can also contribute to the difference between CW and CCW losses.

The percentage variations of the power loss densities per cycle are compared to the stress-free case for each measurement by

$$\Delta p = \frac{p(\sigma_{\mathrm{xx}}, \sigma_{\mathrm{yy}}, \sigma_{\mathrm{xy}}) - p(0, 0, 0)}{p(0, 0, 0)} \tag{12}$$

where $p(0, 0)$ and $p(\sigma_{\mathrm{xx}}, \sigma_{\mathrm{yy}}, \sigma_{\mathrm{xy}})$ represent the loss densities for the stress-free and stressed cases, respectively. Note that for all the studied stress cases, $\sigma_{\mathrm{xy}} = 0$. In Fig. 11, Δp for each measurement case is shown. As expected, an analogy is observed between the loss variations and $\|\boldsymbol{H}\|_{\mathrm{rms}}$ under stress. Considering the effect of uniaxial stress, tension along rolling (x) direction increased the losses, whereas low tensile stress along transverse (y) direction decreased the losses slightly. When uniaxial compressive stress is applied along rolling direction losses increased more than when the compression is applied along transverse direction. Considering multiaxial stress states, low bitensile stress slightly decreased, whereas bicompressive and high bitensile stresses increased the losses slightly. Pure shear stress increased the losses significantly. The effect of stress on the losses is more distinct at low induction amplitudes.

Concerning the uniaxial stress dependence of the rotational losses, different results were reported in the literature for different grades of non-oriented electrical steels. For instance, in [12], the losses under 0.6 and 1 T circular flux densities decreased from the zero-stress condition under uniaxial tension up to around 40 MPa amplitude which was applied along rolling direction, but higher tensile stress levels and compression increased the losses. In [15], it was shown that under 0.8 T circular flux density, rotational losses increased when uniaxial tensile and compressive stress was applied along the rolling direction, whereas low tensile stress along transverse direction reduced the losses slightly. In addition, in [16], it was reported that rotational losses increased under each studied uniaxial tensile and compressive stress applied along the rolling direction under 1 T induction level. The results obtained in this paper are consistent with [15] and [16].

B. Alternating Magnetization Results

The percentage variations of the iron losses compared to the stress-free case are calculated according to (12) for the alternating magnetization with 1.2 T induction level along the x- and y-directions. The results are shown in Fig. 12. When uniaxial tensile stress is applied parallel to the magnetization direction, a decrease in the losses is observed. On the other hand, compression parallel to the magnetization
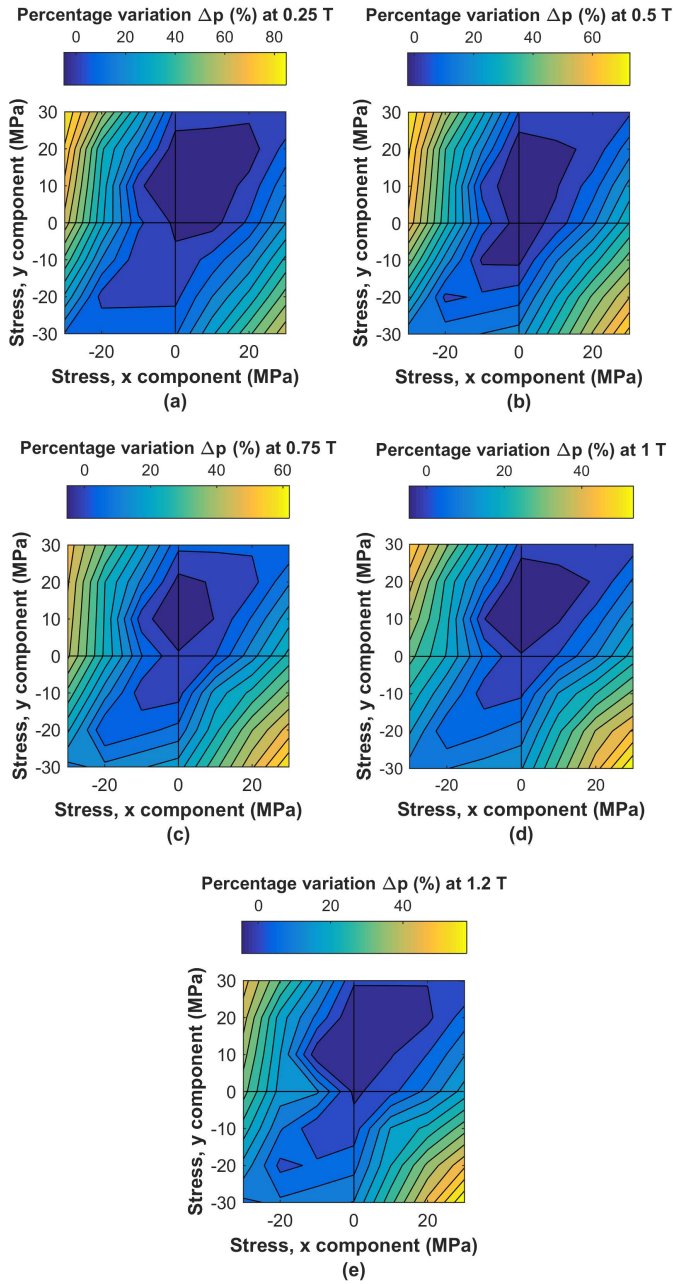
Fig. 11. Measured rotational power loss density variations with respect to stress-free case (Δp) for each stress state and under (a) $\|\boldsymbol{B}\| = 0.25$ T, (b) $\|\boldsymbol{B}\| = 0.5$ T, (c) $\|\boldsymbol{B}\| = 0.75$ T, (d) $\|\boldsymbol{B}\| = 1$ T, and (e) $\|\boldsymbol{B}\| = 1.2$ T induction levels. Note that the scales for each figure are different.

Fig. 12. Measured alternating power loss density variations with respect to stress-free case (Δp) for each stress state with 1.2 T induction level (a) at rolling (x) direction and (b) at transverse (y) direction.

Fig. 13. Measured alternating coercive field variations with respect to stress-free case (H_c) for each stress state with 1.2 T induction level (a) at rolling (x) direction and (b) at transverse (y) direction.

direction increases the losses. The effect is opposite when the uniaxial stress is applied perpendicular to the magnetization direction for both cases. Concerning the biaxial stress states, bicompression and pure shear stress when σ_{xx} is negative (second quadrant) increase the losses when the sample is magnetized along the x-direction. The highest increase in the losses is observed at this pure shear case when σ_{xx} is negative under this magnetization state. On the other hand, bitension and pure shear σ_{xx} being positive (fourth quadrant) decrease the losses when the sample is magnetized along the x-direction. When the sample is magnetized along the y-direction, the effect of biaxial stress states is opposite to that
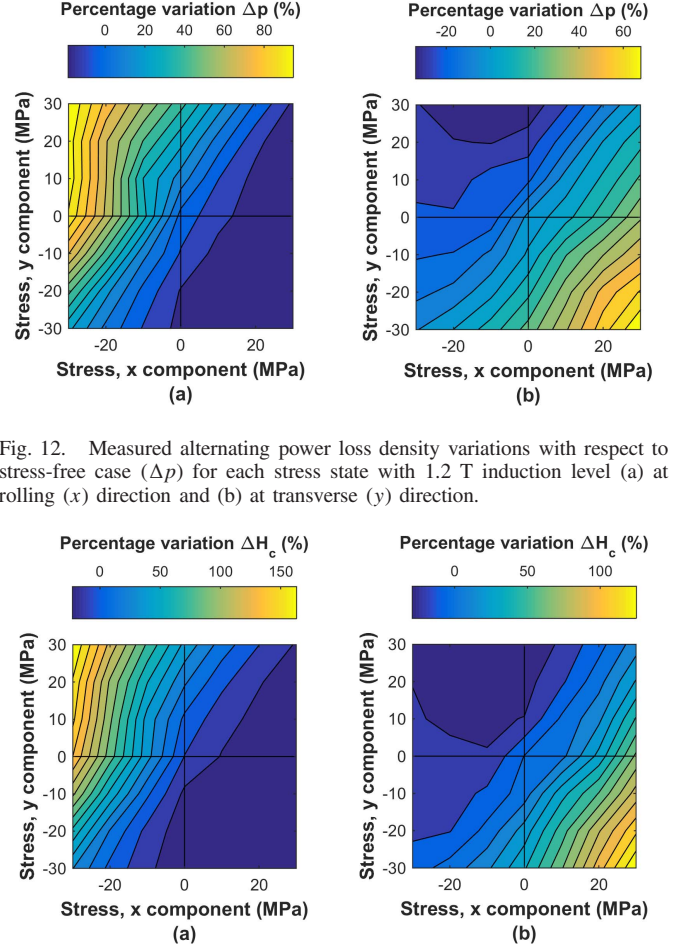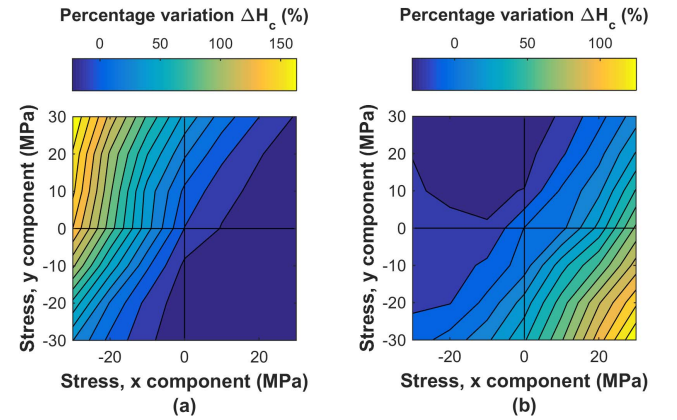
observed when magnetizing along the x-direction. A symmetry between Fig. 12(a) and (b) with respect to $\sigma_{xx} = -\sigma_{xx}/2$ line would be expected with an ideally isotropic material. However, for the studied material, this is not the case since the application of identical uniaxial stresses along the x- or y-directions affect the material differently. This was observed under rotational magnetization condition as well.

In Fig. 13, the percentage variations of the coercive field compared to stress-free case are shown. These variations are calculated for each measurement similar to (12) as

$$\Delta H_c = \frac{H_c(\sigma_{xx}, \sigma_{yy}, \sigma_{xy}) - H_c(0,0,0)}{H_c(0,0,0)}. \quad (13)$$

An analogy between loss and coercive field variations is observed. Similar results were reported, for instance, in [12], [16], [18], and [19].

C. Repeatability of the Measurements

In order to test the repeatability of the measurements, few measurements under zero stress and various uniaxial and biaxial stress configurations were repeated after dismantling and assembling the sample again. Studied stress configurations are shown in Fig. 7 with dot markers. Both rotating and alternating field cases were studied. The studied peak induction

levels were 1 and 1.2 T for rotational and alternating fields, respectively. Considering the stress-free case, the maximum differences between the newer and the older measurements for the loss and field strength were 7.44% and 8.44% under rotating and 3.70% and 5.83% under the alternating field, respectively. As stated in [40], usually the accuracy of an RSST without stress application is not better than 7%. Indeed, including the stressing mechanism to the system increased the maximum differences for the loss and field strength to 11.75% and 14.4% under rotating and 4.19% and 8.39% under alternating field, respectively. Some of the sources that can affect the repeatability are the alignment of the force actuators with respect to the sample, orientation of the rolling and transverse directions of the specimen with respect to the force actuators, ambient temperature, and friction between the sample, sample holder and reinforcing plates, wear and tear of the components. Detailed repeatability and uncertainty analysis of the presented measurement system are complex and lengthy tasks and will be a part of future work.

V. Conclusion

A new RSST device dedicated to test the multiaxial magneto-mechanical behavior of ferromagnetic sheets is introduced by explaining the design phases of the device. The applicability of the device is tested on an M400-50A grade electrical steel sheet. Results under controlled circular and alternating flux density and under several multiaxial stress states are reported. The results show that the effect of multiaxial stress on the rotational and alternating core losses can be much more significant than that of uniaxial stress. Therefore, it is clear that in order to design higher efficiency machines, the effect of multiaxial stress on the material should be considered. In order to do that, accurate models can be created by analyzing the measurement results in detail. In future work, measurements under several excitation frequencies and higher stress magnitudes will be made. In addition, magnetostriction under multiaxial stress will be measured.

Acknowledgment

References

[1] Y. Kai, Y. Tsuchida, T. Todaka, and M. Enokizono, "Evaluation of local residual stress distribution of stator core in rotating machine," *IEEJ Trans. Fundam. Mater.*, vol. 131, no. 5, pp. 389–394, May 2011.

[2] P. Baudouin, A. Belhadj, F. Breaban, A. Deffontaine, and Y. Houbaert, "Effects of laser and mechanical cutting modes on the magnetic properties of low and medium Si content nonoriented electrical steels," *IEEE Trans. Magn.*, vol. 38, no. 5, pp. 3213–3215, Sep. 2002.

[3] D. J. B. Smith, B. C. Mecrow, G. J. Atkinson, A. G. Jack, and A. A. A. Mehna, "Shear stress concentrations in permanent magnet rotor sleeves," in *Proc. Int. Conf. Elect. Mach. (ICEM)*, Rome, Italy, Sep. 2010, pp. 1–6.

[4] F. Chai, Y. Li, P. Liang, and Y. Pei, "Calculation of the maximum mechanical stress on the rotor of interior permanent-magnet synchronous motors," *IEEE Trans. Ind. Electron.*, vol. 63, no. 6, pp. 3420–3432, Jun. 2016.

[5] A. Borisavljevic, H. Polinder, and J. A. Ferreira, "On the speed limits of permanent-magnet machines," *IEEE Trans. Ind. Electron.*, vol. 57, no. 6, pp. 220–227, Jan. 2010.

[6] D. Gerada, A. Mebarki, N. L. Brown, K. J. Bradley, and C. Gerada, "Design aspects of high-speed high-power-density laminated-rotor induction machines," *IEEE Trans. Ind. Appl.*, vol. 58, no. 9, pp. 4039–4047, Sep. 2011.

[7] N. Leuning, S. Steentjes, M. Schulte, W. Bleck, and K. Hameyer, "Effect of elastic and plastic tensile mechanical loading on the magnetic properties of NGO electrical steel," *J. Magn. Magn. Mater.*, vol. 417, pp. 42–48, Nov. 2016.

[8] O. Perevertov, J. Thielsch, and R. Schäfer, "Effect of applied tensile stress on the hysteresis curve and magnetic domain structure of grain-oriented transverse Fe-3%Si steel," *J. Magn. Magn. Mater.*, vol. 385, pp. 358–367, Jul. 2015.

[9] O. Perevertov, "Influence of the applied elastic tensile and compressive stress on the hysteresis curves of Fe-3%Si non-oriented steel," *J. Magn. Magn. Mater.*, vol. 428, pp. 223–228, Apr. 2017.

[10] M. LoBue, C. Sasso, V. Basso, F. Fiorillo, and G. Bertotti, "Power losses and magnetization process in Fe–Si non-oriented steels under tensile and compressive stress," *J. Magn. Magn. Mater.*, vols. 215–216, pp. 124–126, Jun. 2000.

[11] Y. Kai, Y. Tsuchida, T. Todaka, and M. Enokizono, "Influence of stress on vector magnetic property under alternating magnetic flux conditions," *IEEE Trans. Magn.*, vol. 47, no. 10, pp. 4344–4347, Oct. 2011.

[12] V. Permiakov, A. Pulnikov, L. Dupre, and J. Melkebeek, "Rotational magnetization in nonoriented Fe-Si steel under uniaxial compressive and tensile stress," *IEEE Trans. Magn.*, vol. 40, no. 4, pp. 2760–2762, Jul. 2004.

[13] C. Krell, N. Baumgartinger, G. Krismanic, E. Leiss-Holzinger, and H. Pfützner, "Stress effects on the multidirectional magnetic behaviour of grain-oriented silicon iron sheets," *J. Magn. Magn. Mater.*, vols. 215–216, pp. 63–65, Jun. 2000.

[14] Y. Kai, Y. Tsuchida, T. Todaka, and M. Enokizono, "Development of system for vector magnetic property measurement under stress," *J. Elect. Eng.*, vol. 61, no. 7, pp. 77–80, 2011.

[15] Y. Kai, "Measurement of vector magnetic property under stress along arbitrary direction in non-oriented electrical steel sheet," *Przegląd Elektrotechniczny*, vol. 87, no. 9b, pp. 101–105, 2011.

[16] Y. Kai, Y. Tsuchida, T. Todaka, and M. Enokizono, "Influence of stress on vector magnetic property under rotating magnetic flux conditions," *IEEE Trans. Magn.*, vol. 48, no. 4, pp. 1421–1424, Apr. 2012.

[17] M. Rekik, O. Hubert, and L. Daniel, "Influence of a multiaxial stress on the reversible and irreversible magnetic behaviour of a 3% Si-Fe alloy," *Int. J. Appl. Electromagn. Mech.*, vol. 44, nos. 3–4, pp. 301–315, Mar. 2014.

[18] Y. Kai, Y. Tsuchida, T. Todaka, and M. Enokizono, "Influence of biaxial stress on vector magnetic properties and 2-D magnetostriction of a nonoriented electrical steel sheet under alternating magnetic flux conditions," *IEEE Trans. Magn.*, vol. 50, no. 4, Apr. 2014, Art. no. 6100204.

[19] J. Pearson, P. T. Squire, M. G. Maylin, and J. G. Gore, "Apparatus for magnetic measurements under biaxial stress," *IEEE Trans. Magn.*, vol. 36, no. 5, pp. 3599–3601, Sep. 2000.

[20] O. Hubert, F. S. Mballa-Mballa, S. He, and S. Depeyre, "Influence of biaxial stress on magnetic behavior of dual-phase steel-experiments and modeling," *IEEE Trans. Magn.*, vol. 52, no. 5, May 2016, Art. no. 6201004.

[21] Y. Kai, M. Enokizono, and Y. Kido, "Influence of shear stress on vector magnetic properties of non-oriented electrical steel sheets," *Int. J. Appl. Electromagn. Mech.*, vol. 44, nos. 3–4, pp. 371–378, Mar. 2014.

[22] Y. Kai and M. Enokizono, "Effect of arbitrary shear stress on vector magnetic properties of non-oriented electrical steel sheets," *IEEE Trans. Magn.*, vol. 53, no. 11, May 2017, Art. no. 17282713.

[23] A. Basak, A. J. Moses, and R. Al-Bir, "Effect of clamping stress on power loss in POWERCORE strip and Si-Fe transformer cores," *IEEE Trans. Magn.*, vol. 26, no. 5, pp. 1999–2001, Sep. 1990.

[24] A. J. Moses and H. Rahmatizadeh, "Effects of stress on iron loss and flux distribution of an induction motor stator core," *IEEE Trans. Magn.*, vol. 25, no. 5, pp. 4003–4005, Sep. 1989.

[25] S. Zeze, Y. Kai, T. Todaka, and M. Enokizono, "Vector magnetic characteristic analysis of a PM motor considering residual stress distribution with complex-approximated material modeling," *IEEE Trans. Magn.*, vol. 48, no. 11, pp. 3352–3355, Nov. 2012.

[26] K. Yamazaki and Y. Kato, "Iron loss analysis of interior permanent magnet synchronous motors by considering mechanical stress and deformation of stators and rotors," *IEEE Trans. Magn.*, vol. 50, no. 2, Feb. 2014, Art. no. 7022504.

[27] D. Miyagi, N. Maeda, Y. Ozeki, K. Miki, and N. Takahashi, "Estimation of iron loss in motor core with shrink fitting using FEM analysis," *IEEE Trans. Magn.*, vol. 45, no. 3, pp. 1704–1707, Mar. 2009.

[28] K. Delaere, W. Heylen, R. Belmans, and K. Hameyer, "Comparison of induction machine stator vibration spectra induced by reluctance forces and magnetostriction," *IEEE Trans. Magn.*, vol. 38, no. 2, pp. 969–972, Mar. 2002.

[29] L. Bernard and L. Daniel, "Effect of stress on magnetic hysteresis losses in a switched reluctance motor: Application to stator and rotor shrink fitting," *IEEE Trans. Magn.*, vol. 51, no. 9, May 2015, Art. no. 7002513.

[30] U. Aydin, P. Rasilo, D. Singh, A. Lehikoinen, A. Belahcen, and A. Arkkio, "Coupled magneto-mechanical analysis of iron sheets under biaxial stress," *IEEE Trans. Magn.*, vol. 52, no. 3, Mar. 2016, Art. no. 2000804.

[31] J. Sievert, "Two-dimensional magnetic measurements-history and achievements of the workshop," *Przegląd Elektrotechniczny*, vol. 87, no. 9b, pp. 2–10, 2011.

[32] Y. Guo, J. G. Zhu, J. Zhong, H. Lu, and J. X. Jin, "Measurement and modeling of rotational core losses of soft magnetic materials used in electrical machines: A review," *IEEE Trans. Magn.*, vol. 44, no. 2, pp. 279–291, Feb. 2008.

[33] D. Singh, F. Martin, P. Rasilo, and A. Belachen, "Magnetomechanical model for hysteresis in electrical steel sheet," *IEEE Trans. Magn.*, vol. 52, no. 11, Jul. 2016, Art. no. 7301109.

[34] J. J. Zhong, Y. G. Guo, Z. W. Lin, and J. G. Zhu, "Characteristics of soft magnetic composite material under rotating magnetic fluxes," *J. Magn. Magn. Mater.*, vol. 299, pp. 29–34, Apr. 2006.

[35] S. Zurek and T. Meydan, "Errors in the power loss measured in clockwise and anticlockwise rotational magnetisation. Part 1: Mathematical study," *IEE Proc.-Sci., Meas. Technol.*, vol. 153, no. 4, pp. 147–151, Jul. 2006.

[36] K. Matsubara, N. Takahashi, K. Fujiwara, T. Nakata, M. Nakano, and H. Aoki, "Acceleration technique of waveform control for single sheet tester," *IEEE Trans. Magn.*, vol. 31, no. 6, pp. 3400–3402, Nov. 1995.

[37] A. Visioli, "Tuning of PID controllers with fuzzy logic," *IEE Proc.-Control Theory Appl.*, vol. 148, no. 1, pp. 1–8, Jan. 2001.

[38] Z. Jinhua, Z. Jian, D. Haifeng, and W. Sun'an, "Self-organizing genetic algorithm based tuning of PID controllers," *Inf. Sci.*, vol. 179, pp. 1007–1018, Mar. 2009.

[39] O. Hubert, L. Daniel, and R. Billardon, "Experimental analysis of the magnetoelastic anisotropy of a non-oriented silicon iron alloy," *J. Magn. Magn. Mater.*, vols. 254–255, no. 1, pp. 352–354, 2003.

[40] S. Zurek, "Two-dimensional magnetisation problems in electrical steels," Ph.D. dissertation, Wolfson Centre Magn. Technol., Cardiff Univ., Whales, U.K., Mar. 2005.

[41] W. Salz and K. A. Hempel, "Which field sensors are suitable for a rotating flux apparatus," in *Proc. 1st Int. Work. Magn. Properties Elect. Sheet Steel Under Two-Dimensional Excitons*, Braunschweig, Germany, Apr. 1992, pp. 117–126.

[42] K. Mori, S. Yanase, Y. Okazaki, and S. Hashi, "2-D magnetic rotational loss of electrical steel at high magnetic flux density," *IEEE Trans. Magn.*, vol. 41, no. 10, pp. 3310–3312, Oct. 2004.